Resonant carrier dynamics in strongly biassed superlattices

Pavel Abumov[1,2] **and D. W. L. Sprung**[1]

[1] Department of Physics and Astronomy, McMaster University, Hamilton, Ontario L8S 4M1 Canada

[2] Department of Electrical Engineering, University of California, Santa Cruz 98800 CA

E-mail: pabumov@ucsc.edu

Abstract. We study coherent electron dynamics in a biassed undriven ideal semiconductor superlattice coupled to the continuum, near energy level anticrossings. In particular, we examine the dependence of wavepacket dynamical characteristics on electric field detuning, and investigate mixed regimes involving a superposition of energy level anticrossings showing both Rabi oscillations and resonant tunnelling. In earlier work [Phys. Rev. B **75** 165421 (2007)], Rabi and Zener resonances were shown to have a common origin, and a criteria for the occurrence of either was proposed. The present results allow a better understanding of the nature of an interminiband resonance, which can be useful in the areas of microwave radiation generation and matter manipulation on the particle level, as well as demonstrate an alternative approach to examining electron level structure of a finite superlattice.

PACS numbers: 73.23.-b, 73.21.Cd, 78.20.Bh, 78.30.Fs

Submitted to: *J. Phys.: Condens. Matter*

1. Introduction

Carrier dynamics in a biassed superlattice (SL) has remained an active topic during the last two decades. Knowledge of the underlying physical processes is necessary for a better understanding of perpendicular transport of carriers in multi-quantum well systems, as well as for successful development of applications, such as microwave radiation generation [1, 2, 3, 4], quantum computing [5, 6] and matter manipulation on the particle level [7].

Studies focussed on coherent carrier dynamics have revealed some dynamical features of great interest (see, for example, [8] and references therein) arising from the interplay between interminiband oscillations and tunnelling to the continuum. These studies contribute to understanding of the famous quantum-mechanical problem of tunnelling in presence of dissipation [9, 10, 11] that has been considered for superlattices in [12].

Whereas typically such studies involve a number of approximations, we adopted a computational approach with few limitations beyond those implicit in the model of a single electron in a biassed periodic potential. This enabled us to consider resonant dynamics at high and moderate bias in a finite superlattice, specifically Rabi oscillations (RO) and resonant tunnelling (RT), and to establish a relation between these two fundamental types of interminiband transport by simple means. A carrier dynamics solution relying on wavepacket time evolution also brings out certain features that are difficult to calculate otherwise, such as carrier behaviour in the vicinity of a resonance, and dependence of the period of Rabi oscillations on resonance index.

The main purpose of this paper is to further analyze and explain the results obtained using the methods of our earlier work [13]. In particular, our approach helps to study near-resonance behaviour in more detail and understand the damping mechanism of RO and ways to reduce it. It also contributes to a link between RO and RT, an instance where quantum transport theory has been lacking to date. These results can be applied to any system possessing a Wannier-Stark ladder structure including photonic crystals [14] and optical lattices [15].

2. Resonant interminiband dynamics

This work focusses on longitudinal motion of a single electron in a zero-temperature biassed superlattice. We solve the time-dependent Schrödinger equation (TDSE) for $\Psi(x,t)$ in a biassed periodic potential

$$\begin{aligned} V(x) &= \sum_{n=-\infty}^{\infty} V_{SL}(x-nd) + xF \ , \qquad \text{where} \\ V_{SL}(x) &= \frac{V_0}{2}\Big[\tanh\frac{x+a/2}{\sigma} - \tanh\frac{x-a/2}{\sigma}\Big]\Theta(x)\,\Theta(d-x) \ . \end{aligned} \tag{1}$$

where $\Theta(x)$ is the Heaviside function vanishing for $x<0$, $F=-eE$ is a uniform bias, E is the electric field, and $V_{SL}(x)$ is the model superlattice potential in a unit cell of

the periodic system, with width d and barrier thickness a.

We consider coherent electron transport and thus omit electron scattering and relaxation processes; numerous studies of carrier coherency limits have been done in the past [16, 17]. These destructive processes are weak enough at low temperatures, to allow up to 14 Rabi oscillations to occur [18].

Several GaAs/$Ga_{1-x}Al_xAs$ layered heterostructures labelled $X = A$, B, C, D are considered, whose parameters are shown in Table 1 and their band structure in Figure 1. The layer profile function V_{SL} avoids discontinuities in the potential, which allows easier programming of the solver, and is more realistic than the often used square barrier approximation. Our numerical solutions of Equation 1 use discrete transparent boundary conditions [19], which reduces the size of the space domain in which we must operate. For details, see reference [13].

The norm of the quasibound part of the wavepacket ρ and miniband occupancy ρ_ν are convenient properties by which to monitor interminiband dynamics; miniband occupancy is the wavepacket projection onto a tight-binding miniband ν:

$$\rho_\nu = \sum_k |\langle\, \Psi(x,t) \,|\, W_\nu^k(x) \,\rangle|^2 \ .$$

Here $W_\nu^k(x)$ stands for a Wannier-Stark (WS) quasibound state corresponding to energy level E_ν^k centered on the well with index k, and belonging to miniband ν (ν=1,2, ...); our initial wavepacket is centered on the well with index 0. The tight-binding Wannier functions from miniband ν are denoted as $w_\nu(x)$.

To refer to an interminiband resonance originating from an anticrossing of energy levels E_ν^k and E_μ^{k+n} in biassed sample X, we will use the symbol $\mathcal{R}_{\nu\mu}^n(X)$ and we will denote the resonant bias (the value of bias at which the peak of a resonance is observed) as F_n, n being the resonance index (n = 1,2, ...). When of little importance, some indices may be omitted for brevity. For convenience the symbol G will stand for inverse bias $1/F$ ($G_n = 1/F_n$). Unless specified otherwise, time is measured in units of the Bloch period $T_B = 2\pi\hbar/Fd$.

It should be noted that computing a complete complex-energy spectrum for a biassed multilevel system is a significant task beyond the aims of the paper, as can be seen from previous works devoted to this problem (for example, the formalism in [20, 21] utilizes existence of poles of the system scattering matrix). We instead consider a simplified framework proven suitable for the purpose of studying transient transport processes.

2.1. Rabi oscillations model

Typically, Rabi Oscillations (RO) are a result of interminiband transitions under external radiation when its frequency approaches the system's intrinsic value $\omega_{12} = (E_2 - E_1)/\hbar$ [22]. This pumping provides excitation of carriers and their subsequent spontaneous emission of photons, which is widely applied in quantum cascade lasers [23]. A comprehensive overview of RO in the two-miniband approximation has been given

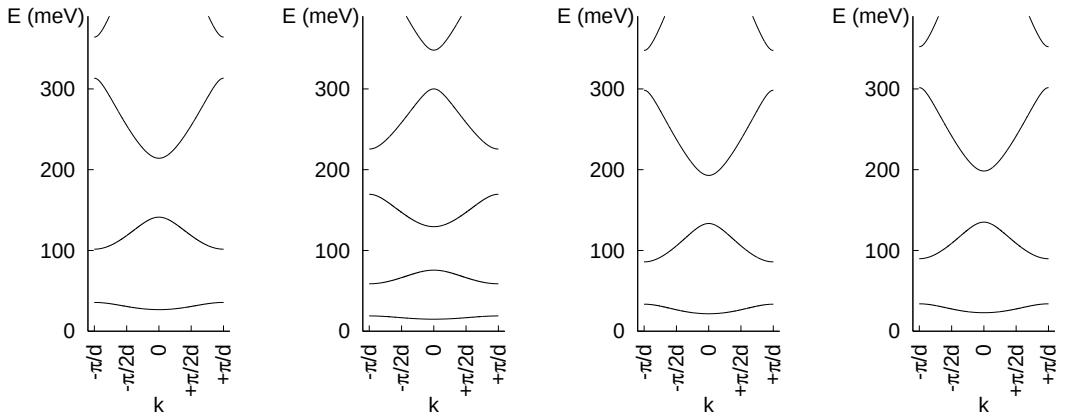

Figure 1. Band structure of the superlattice potentials in absence of bias (from left to right: samples A, B, C and D).

Name	V_0, meV	d, nm(ML)	a, nm(ML)	σ, nm
Sample A	212	13.0 (46)	3.1 (11)	0.4
Sample B	250	17.3 (61)	2.5 (9)	0.4
Sample C	212	13.0 (46)	2.3 (8)	0.4
Sample D	212	13.0 (46)	2.5 (9)	0.4

Table 1. Geometric parameters of the model potentials used in simulations. Barrier height of 212 meV corresponds to x=0.18 and of 250 meV to x=0.3 in the GaAs/$Ga_{1-x}Al_xAs$ structure; ML stands for monolayer thickness, 1 ML = 0.283 nm.

by Ferreira and Bastard [24] and further mathematical details can be found in references [25, 26, 27]. In a biassed SL, interminiband transitions may also occur in the absence of external radiation [28, 29, 30]: when energy levels from coupled Wannier-Stark ladders (WSL) align in neighbouring wells, a carrier can easily tunnel between them.

For an undriven SL (*i.e.* not exposed to an external oscillating electric field) a simplified yet fruitful analogy to an unbiassed system under external radiation can be made. For illustration, consider Bloch oscillations of an electron in a biassed SL, where the electron oscillates in a Bloch domain, with turning points of the motion defined by the edges of a miniband. One can think of this process not as a motion in space, but as oscillation in the local kinetic energy between the upper and lower band edges. For example, let an electron at $t = 0$ have the mean position $\langle x_0 \rangle$ and the fixed initial energy $E_0 = (E_U + E_L)/2$, half way between upper and lower edges, and let a positive bias F be applied in the positive x-direction. An electron moving towards larger values of x will eventually collide with the lower band edge E_L, as the latter rises with slope F. The amplitude of motion in space is $L/2 = (E_0 - E_L)/F = (E_U - E_L)/(2F) \equiv (\delta E/2)/F$,

where δE is the miniband width and L is the Bloch Oscillation (BO) domain width. The two domains, space and energy, are directly related through the bias value F.

Assuming very large carrier lifetime $1/\Gamma$ compared to a typical oscillation period for moderate bias, and taking the WS states to be stationary and orthogonal, we can apply the acceleration theorem $\hbar\,(d\vec{k}/dt) = \vec{F}$, combined with the dispersion relation, to describe wavepacket evolution over a Bloch oscillation cycle. Making use of the decomposition $V(x) = V_{SL} + Fx$ we can write

$$\langle\, x(t)\,\rangle = \frac{1}{\hbar}\int_0^t \frac{dE(k_0 + Ft/\hbar)}{dk}\,dt \tag{2}$$

When the lowest minibands are tightly bound (which is common for a semiconductor SL), carrier dispersion in MBn can be approximated as $E(k) = E_n + (\delta E/2)\cos(kd + n\pi)$ and the mean position evolves as $\langle x(t)\rangle - \langle x(t_0)\rangle = (L/2)\sin\Big(\omega_B(t-t_0)\Big)$, where ω_B is the Bloch angular frequency.

Thus, the local kinetic energy is now time-dependent:

$$\begin{aligned} E\,(t-t_0) &= (E_U + E_L)/2 - F\Big(\langle x(t)\rangle - \langle x(t_0)\rangle\Big) \\ &= E_0 - (FL/2)\,\sin\Big(\omega_B(t-t_0)\Big) \\ &= E_0 - (\delta E/2)\,\sin\Big(\omega_B(t-t_0)\Big)\,. \end{aligned} \tag{3}$$

The wavepacket's evolution in coordinate space at fixed energy can effectively be replaced by its evolution in kinetic energy space. With minor variations, the same viewpoint can be adopted for intrawell oscillations in a similar fashion. Note that the intrawell oscillation frequency is a natural frequency of the system: $\omega_{nm} = (E_m - E_n)/\hbar$.

Given the fact that interminiband transitions of an electron are a result of quantum interference of Bloch and intrawell oscillations [13], one can extend this analogy to Rabi oscillations. Then the SL would be subject to a field of natural frequency ω_{nm}, modulated by the Bloch frequency ω_B. In presence of the ω_{nm} harmonic, this system is poised to undergo an interminiband transition, with a certain Rabi frequency ω_R. This is similar to the well-understood system of a two-level atom under an external monochromatic radiation resonance field f_n. The Schrödinger equation for such a system transforms into

$$\begin{aligned} &-i\hbar\,\frac{\partial\Psi(x,t)}{\partial t} \;=\; (\hat{H}_0 + \hat{V})\,\Psi(x,t) \\ &\text{with}\quad \hat{V} \;=\; \hat{x}\,f_n\,\cos(\omega_R t), \end{aligned} \tag{4}$$

where $\hat{H}_0$ refers to an undriven biassed SL in the tight-binding approximation, $\hat{x}$ is the dipole transition operator between two energy levels (minibands in our case), and f_n is the amplitude of the external electric field.

The factor $\hat{x}f_n$, interpreted as a transition operator in our effective model, represents the strength of interminiband coupling and depends on many factors, including the applied bias and the potential shape. For a small $\hat{x}f_n$, perturbation theory can be applied and an expression for the population of the second level evolving from an initial wavepacket $\Psi(x,0) = W_1(x)$ can then be obtained in the same fashion as for an

irradiated two-level atom. In our notation, for a two-level system driven off its ground state [22] one obtains:

$$\begin{aligned}
&\frac{\rho_2}{\rho}(t) = \Big(\frac{\rho_2}{\rho}\Big)^{max} \mathcal{L}(G)\, \sin^2 \frac{\pi t}{T_R^{max}\sqrt{\mathcal{L}(G)}} \\
&\frac{\rho_1}{\rho}(t) = 1 - \frac{\rho_2}{\rho}(t), \qquad \text{with} \\
&\mathcal{L}(G) \equiv \Big[1 + \Big((G - G_n)/\Gamma\Big)^2\Big]^{-1} \quad \text{where} \\
&\Gamma \quad = x_{0n}/(E_2 - E_1)\ , \\
&T_R^{max} = d/x_{0n}\ , \\
&x_{nm} \quad = \langle\, W_1^n(x)\,|\,x\,|\,W_2^m(x)\,\rangle\ ,
\end{aligned} \tag{5}$$

with n being the index of the resonance considered. These equations are straightforwardly extended to an arbitrary pair of interacting minibands, subject to validity of the perturbation theory used. It is interesting that in order to analytically predict the $\rho_2/\rho\,(t)$ curve in the entire near-resonance region we require only the values of the dipole matrix element x_{nm} and of $(\rho_2/\rho)_{max}$, computed at the resonant bias field.

This simplistic derivation for BO in a two-level tightly bound system applies to the wavepacket's 'centre of mass'. We neglected any change in dispersion of the wavepacket in the process of BO and thus it is only an approximation. Since we consider moderate to high fields in this paper, carrier decay is rapid enough to reduce the influence of this factor. As will be seen in subsequent sections, this simple model provides a surprisingly good fit to the simulation data.

In the case of a strong field, the domain width in space of the wavepacket's 'center-of-mass' BO is typically smaller than a potential cell width. This implies that: (i) energy levels are sparse due to large splitting of WSL; hence near a resonance there is one preferred tunnelling path between MB1 and MB2; (ii) at a resonance, WS states are reasonably localized and have an exponentially vanishing tail, so we expect that $x_{0n} \propto e^{-n}$ (which has been predicted by a two-level atom model [29] and also has been explicitly calculated for a driven multiband SL [20]).

The above argument assumed the system to be in a steady state. However, in practice an initial non-equilibrium configuration undergoes a relaxation process to a state with lower potential energy. We studied the evolution of an initial wavefunction $\Psi(x, t = 0) = c_1 w_1(x) + c_2 w_2(x)$, a linear combination of tight-binding Wannier states. (Obtaining correct quasibound WS functions is not important for our primary goal to study steady-state RO dynamics.) The steady-state tunnelling process showed little dependence on the linear combination: components of $\Psi(x)$ which belong to higher minibands tunnel out rapidly during the initial relaxation period, which only scales down the norm of the quasibound wavepacket being observed. The coefficients c_1 and c_2 should be set so that after an initial period of relaxation of a non-equilibrium state, the resulting RO are clear and of sufficient magnitude. The maximum magnitude of RO between two lowest minibands reaches nearly unity for the two extreme cases $|c_1| = 1$

and $|c_2| = 1$, with less carrier amplitude decay for the former choice. Hence, we adopted the initial wavefunction $\Psi(x, t = 0) = w_1(x)$ for most of our results.

2.2. Near-resonance behaviour

In a Wannier-Stark ladder, energy level anticrossings show a dramatic increase in carrier tunnelling rate, which is ascribed to resonant Zener tunnelling. When studied in detail, carrier dynamics at some of these anticrossings exhibits a prominent oscillatory pattern (Rabi oscillations) which decays rapidly. For clarity we will call the latter Rabi resonances and the others tunnelling resonances. While both are anticrossings of complex energy levels (complex due to their finite width), it will allow us to differentiate the two types. At strong fields, above-barrier tunnelling resonances start to occur; we will include them as tunnelling resonances also.

A study of isolated Rabi resonances in [13] revealed that a carrier undergoing RO produces damped oscillations in miniband occupancy, of the form:

$$\begin{aligned} \rho_n/\rho\,(t) \quad &= P_n + A_R\, e^{-\gamma_A t} \cos\Big(\frac{2\pi t}{T_R} + \phi_n\Big)\,, \\ \text{with} \;\; \rho\,(t) &= \exp\Big(-\gamma t - \sigma\,(1 - e^{-\gamma_{ne} t})\Big) \end{aligned} \tag{6}$$

in agreement with the general theory [31]. Here T_R, A_R and γ_A are the period, amplitude and decay rate of Rabi oscillations respectively; ϕ_n is an initial phase determined by a particular form of $\Psi(x, 0)$ (*e.g.* $\phi_1 \approx 0$ for $\Psi(x, 0) = w_1(x)$); γ is the decay rate of the entire wavepacket and P_n is the asymptotic value of $\rho_n/\rho\,(t)$ in the limit $t \to \infty$. The term $-\sigma\,(1 - e^{-\gamma_{ne} t})$ represents a dip in the decay rate due to two-exponential decay [32] and was found to be vanishingly small close to the resonant bias. Its presence is due to the initial relaxation of wavepacket components orthogonal to eigenfunctions of the current miniband, with σ being proportional to the norm of the orthogonal part and γ_{ne} being the relaxation rate, typically larger by two orders of magnitude than γ. This term compensates for the change in states' orthogonality at higher fields. A typical example of time evolution of near-resonant interminiband occupancy dynamics, and its fit using

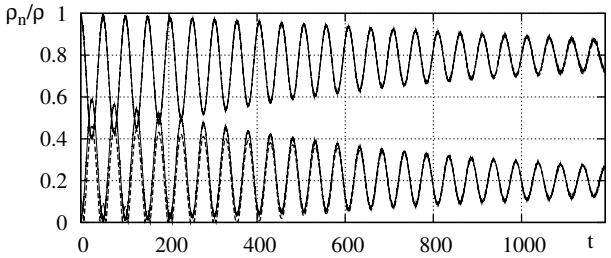

Figure 2. Occupancy functions (solid lines) and their fit using Equation 6 (broken lines almost completely hidden behind them) for $\Psi(x, 0) = w_1(x)$ near a resonance $\mathcal{R}^3_{12}(\mathbf{A})$ at $G = 0.44058$ nm/meV (0.8 HWHM away from the resonant bias); the upper curve corresponds to $n = 1$ and the lower to $n = 2$.

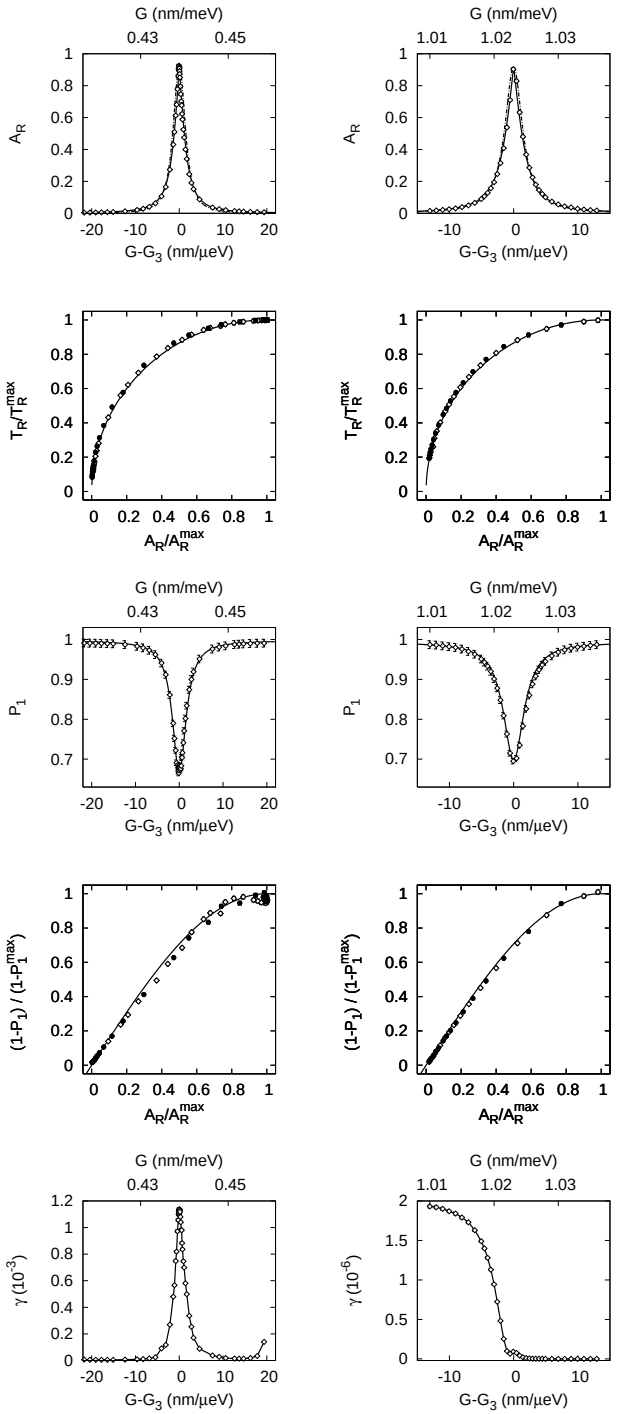

Figure 3. Behaviour of key dynamical parameters for $\mathcal{R}^3_{12}(\mathbf{A})$ (left column) and $\mathcal{R}^3_{12}(\mathbf{B})$ (right column). Top panel shows RO amplitude vs. inverse bias (chain-dotted line shows a Lorentzian fit $\mathcal{L}(G)$, solid line shows fit using Equation 9), second from top panel: relative RO amplitude vs. relative RO period (filled circles correspond to $G < G_3$, empty circles to $G > G_3$; solid line shows fit using Equation 9 given Equation 7), third from top panel: asymptotic occupancy of the first miniband vs. inverse bias (solid line shows fit using Equation 9), fourth from top panel: relative RO period vs. asymptotic occupancy of the first miniband (filled circles correspond to $G < G_3$, empty circles to $G > G_3$; solid line shows fit using Equation 9); bottom panel: carrier decay rate vs. inverse bias.

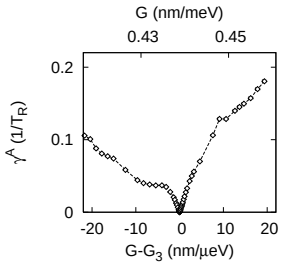

Figure 4. Damping rate of RO vs. inverse bias for $\mathcal{R}^3_{12}(\mathbf{A})$, in units of $1/T_R$.

Equation 6 is shown in Figure 2.

Since the parameters in Equation 6 provide a good description of carrier dynamics for moderate bias, and we will investigate their behaviour near a resonance. It has been found previously [13] that the period T_R of Rabi oscillations shows a root-Lorentzian peak around the resonant bias:

$$T_R(G) = T_R^{max}\sqrt{\mathcal{L}(G)}\,, \tag{7}$$

with the Lorentzian $\mathcal{L}$ defined in Equation 5. We will refer to the parameter Γ of this Lorentzian as the HWHM (half-width at half-maximum) of the resonance under consideration. It has also been shown that the peak period of Rabi oscillations changes exponentially with resonance index n:

$$T_n^{max} = T_1^{max}\Big(T_2^{max}/T_1^{max}\Big)^{n-1}\,.$$

For a double quantum well system, perturbation theory predicts that the frequency of Rabi oscillations strictly at resonant bias is given by $\hbar\omega_R/2 = \langle\,\Psi_L\,|\,V(x)\,|\,\Psi_R\rangle$, the tunnelling matrix element through the barrier separating the two wells [31] and is essentially the splitting between the energy levels. Thus the inverse of T_R^{max} of Equation 7 is the minimum energy level splitting at their anticrossing.

According to these earlier findings, the occurrence of resonant bias values also correlates well with complex energy spectrum anticrossings. As an example, the bias values for anticrossings between two lowest minibands in sample A, obtained from our simulation (G_1=(6.9±0.2) nm/meV, G_2=(3.4±0.2) nm/meV and G_3=(2.33±0.05) nm/meV), are reasonably close to those calculated by K. Hino *et al.* [33] (7.2 nm/meV, 3.6 nm/meV and 2.4 nm/meV, respectively). This agreement demonstrates that interminiband motion prevails at complex energy anticrossings.

The parameters A_R and P_n derived from simulation results also have clear extrema. The following equations fit the data quite well (see Figure 3):

$$A_R = A_R^{max}\Big[1-\sqrt{1-\mathcal{L}^n_{\nu\mu}(G)}\Big], \tag{8}$$
$$\tilde{P}_n = \tilde{P}_n^{max}\sin\frac{\pi A_R}{2A_R^{max}},$$

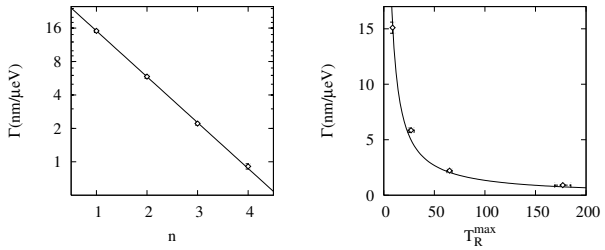

Figure 5. Logarithmic fit of Γ_n versus resonance index for $\mathcal{R}_{12}(\mathbf{A})$ (left) and its relation to T_R^{max} (right).

with A_R^{max} and $\tilde{P}_n^{max}$ being the peak values; $\tilde{P}_n = P_n$ for the lower resonantly coupled MB and $1 - P_n$ for the upper one. The other two parameters, γ and γ_A, are extremely sensitive to coupling to higher minibands and their bias detuning dependence varies from one resonance to another. However, at a resonant bias, γ_A always reached its virtually zero minimum, and γ its maximum (see Figures 3, 4).

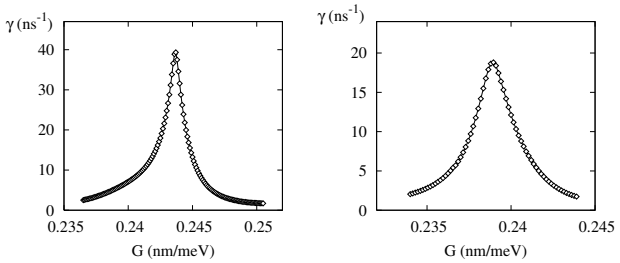

Figure 6. Decay rate γ of a wavepacket vs. inverse bias, near $\mathcal{R}_{13}^5(\mathbf{C})$ (left) and $\mathcal{R}_{13}^6(\mathbf{D})$ (right).

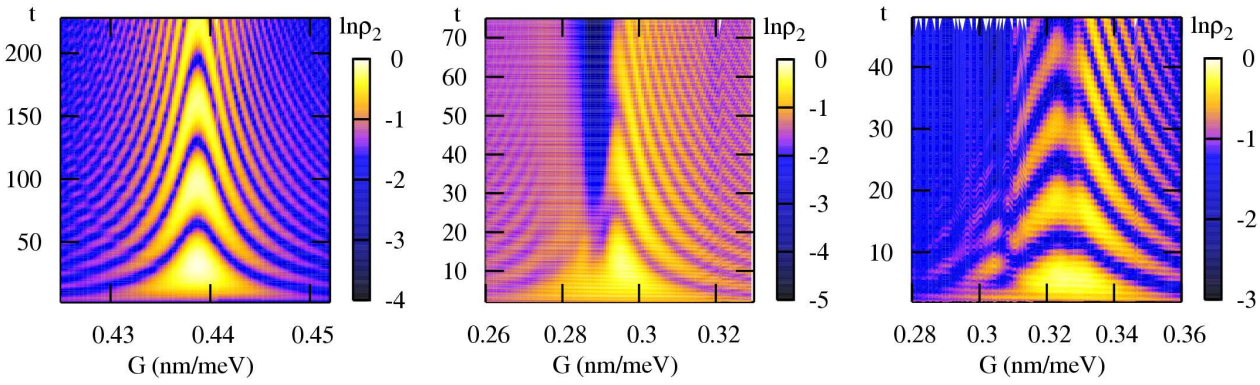

Figure 7. Near-resonant dynamics of second miniband occupancy at $\mathcal{R}_{12}^3(\mathbf{A})$ (left), $\mathcal{R}_{12}^3(\mathbf{C})$ (center) and $\mathcal{R}_{12}^2(\mathbf{B})$ (right).

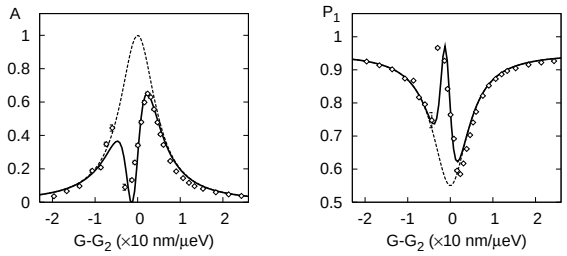

Figure 8. Amplitude of RO and of first miniband occupancy near resonances $\mathcal{R}^2_{12}$ and $\mathcal{R}^5_{13}$ from middle panel of Figure 7. Solid lines show a superposition of Lorentzian curves best fitting simulation data, in circles; broken line is an estimate of a fit in the absence of $\mathcal{R}^5_{13}$.

As the index n rises, the $\mathcal{R}^n_{\mu\nu}$ are expected to narrow, since the length of the tunnelling pathway into the adjacent miniband increases and so does the system's sensitivity to bias detuning, due to related frequency detuning of the Bloch oscillations; this is reflected in a decrease of x_{0n} in Equation 5. As predicted by Equation 5, the resonance HWHM dependence on n closely follows an exponential law (Figure 5) with

$$\Gamma_n = \Gamma_1 \left(\Gamma_2/\Gamma_1\right)^{n-1} \tag{9}$$

The anticipated relation

$$T_n^{max} = G_0/\Gamma_n \tag{10}$$

also holds quite well: fitting Equation (9) produced a value $T_n^{max}\Gamma_n$ =(139 ± 5) nm/μeV compared to G_0 =(145 ± 1) nm/μeV for sample A, and calculations for sample B showed that $T_3^{max}\Gamma_3$ =(1.05 ± 0.01) nm/meV compared to G_0 =(1.02 ± 0.01) nm/meV.

When an ensemble of resonantly coupled minibands is weakly bound, Rabi oscillations are weak and overdamped and it is mostly resonant tunnelling that is seen [34, 35, 36] to prevail over RO; these represent tunnelling resonances. In this case the carrier wavepacket escapes to the continuum very quickly and exhibits no persistent RO. Then γ becomes the key parameter in the dynamical description and features a clear peak centered at the resonant bias (Figure 6). Sensitivity of γ to coupling to higher minibands makes the shape of curves $\gamma(G)$ vary for different resonances.

While we have used perturbation theory to interpret our calculated results, the good fits obtained by using Equations (9,10) suggest that the model remains valid at strong biases as well. We attribute this to the fact that the structure of the Wannier-Stark ladder is preserved over the bias domain considered [13]. At stronger electric fields, however, Bloch oscillations are replaced by sequential tunnelling, and projection on minibands refers merely to the wavepacket's distribution in energy (and hence between wells in real space), rather than a decomposition into Wannier-Stark states. Indeed, the n^{th} tight-bound miniband contains only harmonics with wavelengths $\lambda \in [\frac{n}{2}d, \frac{n+1}{2}d]$.

3. Superposition of carrier dynamical patterns

So far we have considered isolated interminiband resonances. They occur typically in a strong potential at moderate fields where resonances have narrow HWHM compared to their spacing in inverse bias space, and hence they rarely overlap. It is instructive, however, to consider higher-field resonances in a weaker potential (*e.g.* $Al_{0.3}Ga_{0.7}As$, sample B in Table 1), where the interaction between the two resonantly coupled minibands represents only one of several prominent interference paths. Under these conditions, the interaction between these paths becomes important and largely determines the overall dynamics. This gives rise to some particular dynamical patterns that we interpret as interference of tunnelling and Rabi resonances, between different pairs of minibands situated in close proximity.

3.1. Closely situated resonances

We now consider a case of strongly interfering paths, to illustrate how different dynamics contribute in such a mixed mode, and gain understanding of RO stability. This situation typically occurs when the HWHM of one resonance is large compared to the HWHM of another resonance that is coupled to the higher minibands. Then one dynamical pattern is seen to be superimposed on another, as in the centre panel of Figure 7 where one can see evidence of both oscillatory and tunnelling carrier behaviour. The oscillatory pattern related to the $\mathcal{R}^2_{12}$ resonance, vanishes at the $\mathcal{R}^5_{13}$ peak, and the $P_1(G)$ and $A_R(G)$ curves in Figure 8 demonstrate a sharp extremum resembling a superposition of two Lorentzian-like curves.

It is worth mentioning that, in the centre panel of Figure 7, the tunnelling resonance $\mathcal{R}^5_{13}$ that reaches across three minibands, lies above the barrier height of the SL. This gives it comparable strength to $\mathcal{R}^2_{12}$ acting between adjacent minibands, which significantly alters the Rabi resonance pattern. Clearly, resonances which cross three minibands are much weaker than those that cross just two, and a necessary condition for the former to affect the latter significantly, is strong bias resulting in weak carrier

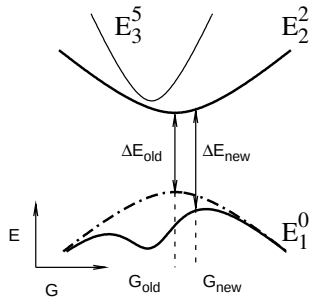

Figure 9. Schematic drawing to illustrate the mutual impact of energy level anticrossings. Chain-dotted line shows position of level E_1^0 in the absence of repulsion from level E_3^5, shown as a thin solid line. For further explanation, see text.

localization. Despite such a strong field, we can use a Wannier-Stark ladder to describe transitions of an electron for the strong fields considered in Figure 7, since the level structure disrupts only at fields high enough for the potential drop per unit cell to be close to the smallest interminiband separation in the system $E_2 - E_1$ [13]. In our case, this value corresponds to the threshold inverse field $G = 0.28$ nm/meV in sample B (the strongest potential considered with smallest $E_2 - E_1$ separation).

In Figure 7 we present a few typical cases of interminiband resonance occurrences. The leftmost panel is an example of an isolated Rabi resonance having an almost perfectly symmetric structure; the two panels to the right are examples of interference between Rabi and tunnelling resonances. In the centre panel, the tunnelling resonance $\mathcal{R}^5_{13}$ appears to be particularly strong and dominating. Hence, to the right of the Rabi resonance $\mathcal{R}^2_{12}$ peak, one sees a clear oscillatory pattern, whereas to the left of the peak it is smeared out by strong tunnelling. The close presence of the tunnelling resonance $\mathcal{R}^5_{13}$ has also the effect of shifting the Rabi resonance $\mathcal{R}^2_{12}$ peak along the bias scale.

From the relation $F_n = n\,F_0$, the resonance $\mathcal{R}^2_{12}$ (centre panel of Figure 7) should have a peak at $G = (0.284 \pm 0.002)$ nm/meV; however as a fit to the maximum period of oscillations indicates, it occurs at a lower bias $G = (0.295 \pm 0.002)$ nm/meV. The shift occurs because at the energy level anticrossing corresponding to $\mathcal{R}^5_{13}$, the levels E^1_0 and E^5_3 are repelled from each other [20]. At the same time, the position of level E^2_2 involved in a Rabi resonance remains almost unchanged. Provided that the minimum mismatch of coupled energy levels $(E^2_2 - E^1_0)$ produces the longest period of RO [13], this results in a shift of the Rabi resonance $\mathcal{R}^2_{12}$ peak as qualitatively shown in Figure 9. There the minimum energy difference at $\mathcal{R}^2_{12}$, ΔE_{old}, located at G_{old} in the absence of a $\mathcal{R}^5_{13}$ anticrossing, shifts to G_{new} due to superposition of the energy level anticrossings $\mathcal{R}^2_{12}$ and $\mathcal{R}^5_{13}$. Since the repulsion from the two anticrossings adds constructively, ΔE_{new} is larger than ΔE_{old}, and since the RO period is inversely proportional to the mismatch in energy level alignment, the peak period of RO shifts to a new value of bias. Thus the proximity of another resonance has a twofold effect on the resonance considered: it shifts its resonant bias and reduces the maximum period of RO. The latter effect is demonstrated in the right panel of Figure 7, where a weak and narrow tunnelling resonance spread over $G = 0.322 \ldots 0.330$ nm/meV reduces the RO period.

3.2. Conditions for Rabi resonance

The simulation data reveal that the decay of RO is slower far from tunnelling resonances and in stronger potentials, with tightly bound lowest minibands reducing the carrier decay rate γ. At the same time, the RO decay rate nearly vanishes at the very peak of a Rabi resonance, where the wavepacket decay rate is at its highest. Thus tunnelling rate alone is not a reliable indicator of Rabi oscillation damping. As Figure 10 demonstrates, resonant tunnelling and Rabi oscillation patterns may occur for the same wavepacket decay rate.

In the centre panel of Figure 7 at inverse bias $G^{(3)} = 0.312$ nm/meV there is a

clear RO pattern, whereas at the bias $G^{(1)} = 0.274$ nm/meV (which is symmetric to $G^{(3)}$ in relation to the Rabi resonance peak located at $G = 0.293$ nm/meV), Rabi oscillations die out quickly. This behaviour goes beyond the symmetric structure of an isolated resonance as in Equation 7 (left panel of Figure 7); it is interference of a tunnelling resonance at $G^{(1)}$ that overdamps the Rabi oscillations. To generalize, the alignment of energy levels from higher minibands sets the wavepacket behaviour model and the link between RO and tunnelling resonance (both being a product of wavepacket self-interference) is determined by a particular arrangement of Wannier-Stark ladders: specifically, by the ratio of interminiband tunnelling rates, as will be argued next.

For illustrative purposes, we turn again to the two-miniband model and denote the rate of tunnelling from MBν to MBμ as $\gamma_{\nu\mu}$; this is a convenient measure of strength of interminiband coupling. The magnitude of $\gamma_{\nu\mu}$ is inversely proportional to the difference in energy between the resonantly coupled energy levels from WSLν and WSLμ [37]. In the centre panel of Figure 7, these level pairs are: E_1^0 and E_2^2 for the Rabi resonance and E_1^0 and E_3^5 for the tunnelling resonance. As seen in Figure 10, for the inverse biases $G^{(2)}$ and $G^{(3)}$ featuring the same carrier decay rate, the difference $(E_2^2 - E_1^0) - \Delta E_{21}$ determining the tunnelling between MB1 and MB2 is -2 meV and 6.2 meV, respectively (ΔE_{21} is the energy spacing between the centres of MB2 and MB1, which equals 88.8 meV for potential A), whereas at the same values of bias, $(E_3^5 - E_1^0) - \Delta E_{31}$ for the ensemble of MB1 and MB3 equals -10 meV and 10 meV. Considering that the widths of the tight-binding MB1, MB2 and MB3 are 8.8, 39.4 and 98.6 meV, the disparity between the two values of $(E_2^2 - E_1^0) - \Delta E_{21} \propto 1/\gamma_{12}$ is much more significant than that of $(E_3^5 - E_1^0) - \Delta E_{31} \propto 1/\gamma_{13}$. Hence, the ratio γ_{12}/γ_{23}, which indicates the isolation of the coupled bands MB1 and MB2 from higher minibands, is much smaller in the case of $G^{(1)}$. Due to a weaker isolation of the ensemble at $G^{(1)}$, the quasibound oscillating part of the wavepacket is more subject to tunnelling into the continuum, so RO are destroyed and turn more quickly into resonant tunnelling. The evidence for this is the middle line in Figure 10 featuring strongly damped oscillations.

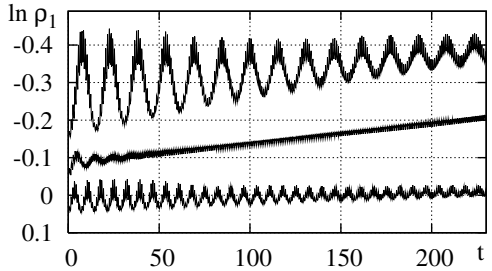

Figure 10. Dynamics of first miniband occupancy in the vicinity of $\mathcal{R}_{12}^2$, from the centre panel of Figure 7 at $G^{(3)} = 0.301$ nm/meV (upper curve), $G^{(2)} = 0.293$ nm/meV (middle curve) and $G^{(1)} = 0.274$ nm/meV (lower curve). The upper [lower] curve is shifted upwards [downwards] by 0.1 for visibility.

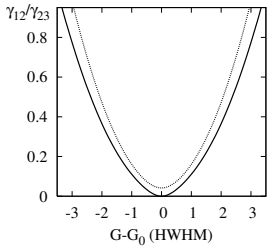

Figure 11. Ratio of interminiband tunnelling rates γ_{12}/γ_{23} vs. inverse bias (in resonance HWHM units), from Equation 11 given Equation 9. Solid and broken lines show the cases when $P_1 = 0.5$ and 0.6 at resonance (ideal and nearly ideal cases), respectively.

This also explains why, at the peak of an isolated Rabi resonance, the RO damping rate is the lowest. For example, at R_{12} two lowest minibands merge through resonant coupling, so γ_{12} and γ are exploding while γ_{23} changes relatively little. In other words, at an anticrossing, the decay rate of a more stable state changes much more than that of a less stable one. Thus, a surging ratio of γ_{12}/γ_{23} makes RO decay go nearly to zero at the peak, despite homogeneous level broadening which reaches its greatest extent there. Away from the peak γ falls off and RO persistence decreases, because of the quick drop in γ_{12} (Figure 4). This is a somewhat counterintuitive example of how a quasibound state with shorter lifetime can produce more prominent oscillations.

Since γ_{12} is closely related to the interminiband transition matrix element V_{12}, we can estimate the near-resonant behaviour of the latter by invoking some dynamical equilibrium considerations. From an elementary two-miniband model (see the Appendix) we obtain

$$\frac{\gamma_{12}}{\gamma_{23}} = \frac{2P_1 - 1}{P_1(1 - P_1)} \tag{11}$$

Neglecting tunnelling pathways between poorly aligned energy levels (*e.g.* $E_1^0 \rightarrow E_2^1$ at $\mathcal{R}_{12}^2$) and over many potential wells (in case of resonance across three minibands), $V_{12} = \gamma_{12}$. Assuming that γ_{23} changes over bias near $\mathcal{R}_{12}$ adiabatically slowly compared to γ_{12}, we get $V_{12} \propto \frac{(2P_1-1)}{P_1(1-P_1)}$; with the fit for $P_1(G)$ from Equation 9, we can estimate the behaviour of V_{12} as shown in Figure 11. In the ideal case of $P_1 = 0.5$ at the peak, γ_{12} vanishes, which reflects a complete merger of the two lowest minibands. This example shows a link between the results obtained for bias detuning dependence of the key dynamical parameters, and theoretical values. With few simplifying approximations, one can investigate near-resonant behaviour of theoretical parameters based on carrier dynamics in a finite superlattice system in the above manner, using a system of coupled damped oscillators described in [38].

3.3. RO damping and quantum interference

On a fundamental level, RO damping may be seen to originate from self-interference of a wavepacket that is facilitated by interference between small fractions of wavefunction that a wavepacket constantly emits through intrawell and Bloch oscillations (we will call them 'ripples'). A wavepacket initially set in the ground miniband of a biassed SL, starts to leak out into the second miniband, since the interference of the 'ripples' is constructive at the location of the initially unpopulated MB2, and destructive at MB1. When most of the wavepacket has tunneled out into MB2, the tunnelling direction reverses. This follows since by then most of the emission is from MB2. In the ideal case of zero RO damping, this reversion is a mirror process; in practice, the tunnelling rate to higher minibands cannot be neglected. This causes the amount of emitted 'ripples' to reduce faster in MB2; such an inequality breaks the mirror symmetry of the two transitions. The oscillation pattern smears out and RO are damped more quickly, the larger is the imbalance in the rate of 'ripples' escaping to the continuum. That is, inversely proportional to γ_{12}/γ_{23}. In other words, if γ_{23} cannot be neglected compared to γ_{12}, it breaks the anisotropy in the system's tunnelling pathways: in addition to MB1$\leftrightarrow$MB2, there appear two additional pathways, MB1$\leftrightarrow$MB3 and MB2$\leftrightarrow$MB3 with very different tunnelling rates.

4. Conclusion

From the results of numerical simulations of near-resonant carrier dynamics at an isolated resonance, we have proposed a set of equations governing wavepacket behaviour; the dynamical parameters near a resonance were found to exhibit extrema of various shapes. For overlapping resonances, a superposition of energy level anticrossings produces a shift in resonant bias. It also reduces the maximum period of RO and perturbs the dependence of dynamical parameters on bias. A superposition of Rabi and tunnelling resonances also allowed us to observe the transition between oscillatory and tunnelling coherent wavepacket dynamics, and to examine the mechanism of RO damping.

Persistence of Rabi oscillations near a resonance was demonstrated to be independent of homogeneous level broadening and to depend on the ratio of interminiband tunnelling rates γ_{12}/γ_{23}, which can serve as an estimate of the RO damping rate.

Acknowledgments

We are grateful to NSERCanada for continuing support under discovery grant RGPIN-3198. We also thank Dr. W. van Dijk for his help in implementing the numerical algorithm. The numerical simulations were carried out on the Shared Hierarchical Academic Research Computing Network (www.sharcnet.ca).

Appendix: dynamical equilibrium for a two-miniband system

We consider an elementary system of two strongly interacting minibands coupled to continuum states. Further, let us denote the tunnelling rate from MBν to MBμ as $\gamma_{\nu\mu}$, from MBν to continuum as $\gamma_{\nu\infty}$ and the current relative occupancy of MBν as $\rho_\nu/\rho \equiv \tilde{\rho_\nu}$. In steady tunnelling mode, the miniband occupancies are in dynamical equilibrium. Neglecting direct tunnelling from MB1 to the continuum, the flow of probability is balanced as follows:

$$\begin{cases} \frac{d}{dt}\vec{\tilde{\rho}} = \begin{pmatrix} \gamma_{12} & -\gamma_{21}-\gamma_{2\infty} \\ -\gamma_{12} & \gamma_{21} \end{pmatrix} \vec{\tilde{\rho}} \\ \frac{d}{dt}\frac{\tilde{\rho_1}}{\tilde{\rho_1}+\tilde{\rho_2}} = -\frac{d}{dt}\frac{\tilde{\rho_2}}{\tilde{\rho_1}+\tilde{\rho_2}} \end{cases}$$

where $\vec{\tilde{\rho}}$ has components $\tilde{\rho}_1$, $\tilde{\rho}_2$, and the second equation expresses the condition for dynamical equilibrium. A little algebra produces the quadratic equation

$$\kappa^2\gamma_{12} - \kappa(\gamma_{21} - \gamma_{12} + \gamma_{2\infty}) - \gamma_{21} = 0$$

with $\kappa = \tilde{\rho_1}/\tilde{\rho_2} > 1$. Taking $\tilde{\rho_2} = 1 - \tilde{\rho_1}$ and assuming $\gamma_{12} \approx \gamma_{21} = \gamma$ (which holds well in the vicinity of a resonance peak), in the steady-state limit $t \to \infty$ we arrive at

$$\alpha = \frac{2P_1 - 1}{P_1(1 - P_1)}$$

with the notation $\alpha = \gamma_\infty/2\gamma$ and $\gamma_\infty = \gamma_{2\infty}$. Note that the extreme case of RT corresponds to $\alpha \to \infty$ with $P_1 \to 1$, and of RO to $\alpha \to 0$ with $P_1 \to 0.5$.

References

[1] Waschke, C., Roskos, H. G., Leo, K., Kurz, H., and Köhler, K. (1994) *Semicond. Sci. Technol.* **9**, 416–418.

[2] Jin, K., Odnoblyudov, M., Shimada, Y., Hirakawa, K., and Chao, K. A. (2003) *Phys. Rev. B* **68(15)**, 153315.

[3] Romanov, Y. A. and Romanova, Y. Y. (2005) *Semiconductors* **39(1)**, 147–155.

[4] Shimada, Y., Sekine, N., and Hirakawa, K. (2004) *Appl. Phys. Lett.* **84(24)**, 580.

[5] Zrenner, A., Beham, E., Stufler, S., Findeis, F., Bichler, M., and Abstreiter, G. (2002) *Nature* **418(6898)**, 612.

[6] Wang, Q. Q., Muller, A., Bianucci, P., Rossi, E., Xue, Q. K., Takagahara, T., Piermarocchi, C., MacDonald, A. H., and Shih, C. K. (2005) *Phys. Rev. B* **72**, 035306.

[7] Breid, B. M., Witthaut, D., and Korsch, H. J. (2007) *New J. Phys.* **9**, 62.

[8] Latge, A., Ribeiro, F. J., Bruno-Alfonso, A., Oliveira, L. E., and Brandi, H. S. (2006) *Braz. J. Phys.* **36(2A)**, 898.

[9] Shah, J. (1999) Ultrafast spectroscopy of semiconductors and semiconductor nanostructures, Springer-Verlag, Berlin and Heidelberg.

[10] Beham, E., Zrenner, A., Stufler, S., Findeis, F., Bichler, M., and Abstreiter, G. (2003) *Physica E* **16(1)**, 59–67.

[11] Vasanelli, A., Ferreira, R., and Bastard, G. (2002) *Phys. Rev. Lett.* **89**, 216804.

[12] Han, P., Jin, K. J., Zhou, Y. L., Zhou, Q. L., Lu, H. B., Guan, D. Y., and Yang, G. Z. Dec 2005 *Europhys. Lett.* **72(6)**, 1011–1017.

[13] Abumov, P. and Sprung, D. W. L. (2007) *Phys. Rev. B* **75**, 165421.

[14] Wilkinson, P. B. (2002) *Phys. Rev. E* **65(5)**, 056616.

[15] Sias, C., Zenesini, A., Lignier, H., Wimberger, S., Ciampini, D., Morsch, O., and Arimondo, E. (2007) *Phys. Rev. Lett.* **98**, 120403.
[16] Eickemeyer, F., Reimann, K., Woerner, M., Elsaesser, T., Barbieri, S., Sirtori, C., Strasser, G., Müller, T., Bratschitsch, R., and Unterrainer, K. (2002) *Phys. Rev. Lett.* **89**, 047402.
[17] Rauch, C., Strasser, G., Unterrainer, K., Wacker, A., and Gornik, E. (1999) *Physica B* **272**, 175.
[18] Roskos, H. G., Nuss, M. C., Shah, J., Leo, K., Miller, D. A. B., Fox, A. M., Schmitt-Rink, S., and Köhler, K. (1992) *Phys. Rev. Lett.* **68**, 2216.
[19] Moyer, C. A. (2004) *Am. J. Phys.* **72(3)**, 352–358.
[20] Glück, M., Kolovsky, A. R., and Korsch, H. J. (2002) *Phys. Rep.* **366**, 103–182.
[21] Glück, M., Kolovsky, A. R., Korsch, H. J., and Zimmer, F. (2002) *Phys. Rev. B* **65**, 115302.
[22] Akulin, V. M. and Karlov, V. V. (1992) Coherent Interaction, Springer-Verlag, Berlin.
[23] Capasso, F. J., Sivco, D. L., Sirtori, C., Hutchinson, A. L., and Cho, A. Y. (1994) *Science* **264**, 553.
[24] Ferreira, R. and Bastard, G. (1997) *Rep. Prog. Phys.* **60**, 345.
[25] Brandi, H. S., Latgé, A., Barticevic, Z., and Oliviera, L. E. (2005) *Sol. State Comm.* **135**, 386–389.
[26] Rotvig, J., Jauho, A.-P., and Smith, H. (1995) *Phys. Rev. Lett.* **74(10)**, 1831.
[27] Glück, M., Hankel, M., Kolovsky, A. R., and Korsch, H. J. (2000) *J. Optics B* **2**, 612–617.
[28] Ferreira, R., Bastard, G., and Voisin, P. (1994) *Solid-State Electronics* **37**, 857.
[29] Bastard, G., Ferreira, R., Chelles, S., and Voisin, P. (1994) *Phys. Rev. B* **50(7)**, 4445.
[30] Bleuse, J., Bastard, G., and Voisin, P. (1988) *Phys. Rev. Lett.* **60(3)**, 220.
[31] Vasko, F. A. and Kuznetzov, A. V. (1999) Electronic states and Optical Transitions in Semiconductor Heterostructures, Springer, New York.
[32] Gurvitz, S. A. and Marinov, M. S. (1989) *Phys. Rev. A* **40(4)**, 2166.
[33] Hino, K., Yashima, K. and Toshima, N. (2005) *Phys. Rev. B* **71**, 115325.
[34] Glutsch, S. (2004) *Phys. Rev. B* **69**, 235317.
[35] Vojvodic, A., Blom, A., Ma, Z. S., Shimada, Y., Hirakawa, K., and Chao, K. A. (2005) *Sol. State Comm.* **136(11-12)**, 580–584.
[36] Konotop, V. V., Kevrekidis, P. G., and Salerno, M. (2005) *Phys. Rev. A* **72(2)**, 023611.
[37] Cohen, G., Gurvitz, S. A., Bar-Joseph, I., Deveaud, B., Bergman, P., and Regreny, A. (1993) *Phys. Rev. B* **47(23)**, 16012.
[38] Leo, K., Shah, J., Gordon, J. P., Damen, T. C., Miller, D. A. B., Tu, C. W., and Cunningham, J. E. (1990) *Phys. Rev. B* **42(11)**, 7065.